



UNIVERSITY OF LEEDS

This is a repository copy of *Visualizing surface plasmons with photons, photoelectrons, and electrons..*

White Rose Research Online URL for this paper:

<http://eprints.whiterose.ac.uk/99371/>

Version: Accepted Version

Article:

EI-Khoury, PZ, Abellan, P, Gong, Y et al. (6 more authors) (2016) Visualizing surface plasmons with photons, photoelectrons, and electrons. *Analyst*, 141 (12). pp. 3562-3572. ISSN 0003-2654

<https://doi.org/10.1039/C6AN00308G>

Reuse

Unless indicated otherwise, fulltext items are protected by copyright with all rights reserved. The copyright exception in section 29 of the Copyright, Designs and Patents Act 1988 allows the making of a single copy solely for the purpose of non-commercial research or private study within the limits of fair dealing. The publisher or other rights-holder may allow further reproduction and re-use of this version - refer to the White Rose Research Online record for this item. Where records identify the publisher as the copyright holder, users can verify any specific terms of use on the publisher's website.

Takedown

If you consider content in White Rose Research Online to be in breach of UK law, please notify us by emailing eprints@whiterose.ac.uk including the URL of the record and the reason for the withdrawal request.

Visualizing Surface Plasmons with Photons, Photoelectrons, and Electrons

P. Z. El-Khoury,^{a,*} P. Abellan,^b Y. Gong,^a F. S. Hage,^b J. Cottom,^c A. G. Joly,^a R. Brydson,^c Q. M. Ramasse,^b and W. P. Hess^a

^aPhysical Sciences Division, Pacific Northwest National Laboratory, Richland, WA 99352, USA;
^bSuperSTEM Laboratory, SciTech Daresbury Campus, Daresbury WA4 4AD, UK; ^cInstitute for Materials Research, School of Chemical and Process Engineering, University of Leeds, Leeds, U.K.

*patrick.elkhouri@pnnl.gov

Abstract

Both photons and electrons may be used to excite surface plasmon polaritons, the collective charge density fluctuations at the surface of metal nanostructures. By virtue of their nanoscopic and dissipative nature, a detailed characterization of surface plasmon (SP) eigenmodes in real space-time ultimately requires joint sub-nanometer spatial and sub-femtosecond temporal resolution. The latter realization has driven significant developments in the past few years, aimed at interrogating both localized and propagating SP modes over the relevant length and time scales. In this mini-review, we briefly highlight different techniques employed by our own groups to visualize the enhanced electric fields associated with SPs. Specifically, we discuss recent hyperspectral optical microscopy, tip-enhanced Raman nano-spectroscopy, nonlinear photoemission electron microscopy, as well as correlated scanning transmission electron microscopy-electron energy loss spectroscopy measurements targeting prototypical plasmonic nanostructures and constructs. Through selected practical examples from our own laboratories, we examine the information content in multidimensional images recorded by taking advantage of each of the aforementioned techniques. In effect, we illustrate how SPs can be visualized at the ultimate limits of space and time.

Brief Overview

The resonant interaction between electromagnetic radiation and surface plasmon (SP) eigenmodes in nanostructured noble metals is a phenomenon of ever-growing interest. SPs have found applications in fields as diverse as ultrasensitive chemical detection and nanoscale chemical imaging, targeted drug delivery and therapeutics, photovoltaics, as well as photocatalysis, to name a few.^{1,2,3} The enhanced electromagnetic fields associated with localized surface plasmons (LSPs) have enabled (i) establishing the chemical identity of a single molecule, through surface-enhanced Raman scattering (SERS),¹ (ii) ultrasensitive nanoscale (bio)chemical imaging, using tip-enhanced Raman spectroscopy (TERS),² and more recently, (iii) the observation of vibrational wavepacket motion on a single molecule in real-time, *via* surface-enhanced coherent anti-Stokes Raman scattering.⁴ Light waves trapped on metallic surfaces in the form of propagating surface plasmons (PSPs) exhibit other unique features that are attractive for on-going quests aimed at constructing mesoscale plasmonic circuitry, with tunable nanometric sub-components.⁵ Because of momentum mismatch, the direct coupling of light waves, incident onto a metal-vacuum interface, into PSP modes cannot be achieved without intermediary coupling designs.⁶ Such motifs include nanoscale lithographic patterns,⁷ which provide an additional source of momentum for coupling light waves into the metal. Subsequently, PSPs can be manipulated over subwavelength length scales,⁸ and even (coherently) transported to distances hundreds of microns away from their initial coupling sites.⁹

Nanometric variations in the structures of SP-supporting constructs may completely alter their overall plasmonic properties. In the context of single molecule SERS and TERS, where the interaction between SP-enhanced local electric fields and molecular polarizability tensors governs the observables, the aforementioned variations obfuscate the analysis of the recorded spectra.¹ The commonly adopted practice of correlating structural/topographic images of plasmonic nanostructures with molecular SERS/TERS spectra is often insufficient; the need for analytical tools that can be used to gain independent access to the SP-enhanced local electric fields presents itself in this context. The latter is one of the major drives behind the works described herein. By virtue of their polaritonic nature,⁶ both photons and electrons may be used to excite and probe SPs, as demonstrated in recent reviews.¹⁰ Of the various techniques of choice, the inherent simplicity and rich information content in far-field techniques based on optical microscopy are attractive. Previous works have demonstrated that a combination of dark field optical microscopy and spectroscopy (dark field micro-spectroscopy) can be used to detect and spectroscopically characterize single plasmonic nanostructures.^{10,11} Motivated and inspired by the prior works, we very recently developed a hyperspectral optical microscope, which allows us to record 3D images (wavelength resolved 2D micrographs) of plasmonic nanostructures.¹² Diffraction-limited hyperspectral dark field optical microscopy constitutes the starting point of our discussion. This is followed by describing another all-optical measurement in which light reflected off a metallic probe of an atomic force microscope reports on SP-enhanced electric fields, with a spatial resolution an order of magnitude finer than the diffraction limit of light. We then discuss time-integrated and time-resolved nonlinear photoemission electron microscopy, whereby nanoscale maps of LSP-enhanced electric fields

are recorded, and PSPs are imaged with joint femtosecond temporal and nanometer spatial resolution. Finally, we describe high resolution electron energy loss spectroscopy measurements that characterize plasmonic fields with joint Ångström spatial and meV energy resolution.

Hyperspectral Dark Field Optical Microscopy of Single Silver Nanospheres

That many physical, chemical, and biological processes can be better understood from single particle studies is a premise that has motivated significant advances in the field of plasmonics.^{1,2,4,10,11} Spectrally resolved optical microscopy is not a novel concept.^{10,11} Our approach to the problem is nonetheless distinct from prior demonstrations. Namely, we rely on the combination of a hyperspectral detector (SOC710-VP, Surface Optics Corporation) equipped with an internal scanning design and a confocal optical microscope (Leica, DM4000M) to record spectrally ($400 \text{ nm} \leq \lambda \leq 1000 \text{ nm}$, $\Delta\lambda < 4.69 \text{ nm}$) and spatially (diffraction-limited, sampled at $85 \text{ nm}^2/\text{pixel}$) resolved optical micrographs. In this scheme, hyperspectral images are obtained by scanning a line detector (at a rate of 30 lines/second) containing 512 pixels ($85 \text{ nm}^2/\text{pixel}$) over the field of view dictated by the microscope objective (herein, 100X, NA=0.75). Each element comprising the aforementioned line contains spectral information in the 400-1000 nm region, at a spectral resolution of 4.69 nm. In principle, our setup allows us to record spectrally resolved transmission, reflection, fluorescence, and dark field optical micrographs. The following is focused on the latter imaging mode. As illustrated below, ample signal-to-noise is obtained, allowing us to analyze both the scattering profiles as well as the optical response of plasmonic nanoparticles. What distinguishes our setup from its previously described

analogues^{10,11} is that it affords multi-modal hyperspectral microscopy without resorting to sample scanning or point by point detection schemes, which (i) are typically more time consuming, which may introduce uncertainties (e.g. as a result of image drifting under ambient laboratory conditions), and (ii) often involve more convoluted setups and subsequent numerical analyses.

Operating our optical microscope in dark field mode allows us to record a real color image of the scattering from an isolated silver nanoparticle (diameter = 100 nm) on glass, see **Figure 1A**. Our goal is to spectrally resolve this dark field optical image using the above-described hyperspectral microscope, as schematically illustrated in **Figure 1B**, and subsequently, to spectrally resolve the SP resonances of individual plasmonic nanoparticles. The information content in a hyperspectral image can be extracted either by analyzing images recorded at different wavelengths and/or by inspecting the optical response contained in each pixel. **Figure 1C** shows the dark field optical image of an isolated silver nanoparticle at 503 nm, a horizontal cross-section of which is plotted in **Figure 1E**. A Gaussian fit of the recorded scattering profile gives a full width at half maximum of 381 nm, consistent with, but somewhat larger than the diffraction-limited ~335 nm value expected based on a numerical aperture of 0.75. The experimental value depends on the choice of physical model used and overall quality of the resulting fit. For instance, the deviation of the Gaussian fit from the experimental profile towards the maximum is noted, see **Figure 1E**. Alternatively, we may analyze the scattering profile of the isolated plasmonic silver nanoparticle using a statistical method which solely relies on intensity counts to examine image texture.¹³ Namely, we opt to apply a texture filter based on a co-occurrence matrix.¹³ Our filter of choice for this demonstration is statistical

variance in a 3x3 pixel window, which is scanned across the recorded image. This allows us to rapidly locate the center and edges (in the diffraction-limited far field image projection) of the isolated scatterer from its hyperspectral dark field image. Namely, applying a variance filter to the 503 nm dark field micrograph shown in Figure 1C yields the filtered image shown in Figure 1D. The 2D scattering profile in the former, best described as a 2D normal distribution, is transformed into a doughnut-shaped spatial distribution in the latter. This is a consequence of low local variance at the center of the scattering profile, as compared to high local variance towards its edges, or more accurately, at the inflection points of the 2D normal intensity distribution. The effect is further bolstered in Figure 1E, where a horizontal cross-section of the variance-filtered image is plotted. Here, the scattering diameter measured from the variance-filtered image as the distance between the two points of highest variance is 340 nm, in close agreement with the theoretical value based on the numerical aperture of the objective used in this measurement.

Applying a variance filter based on a co-occurrence matrix also allows us to rapidly pinpoint the center of the scatterer in 2D, in this case to within one pixel (85 nm^2), see Figures 1D and 1E. Subsequently, the spectra recorded in a 3x3 pixel area around the identified particle center can be extracted from the hyperspectral optical image and averaged, as shown in Figures 1C and 1F. The signal-to-noise achieved in the spatially averaged dark field scattering spectrum enables us to accurately resolve the optical response of a single plasmonic silver nanoparticle, see Figure 1F, which in this case is governed by the SP resonance of the spherical silver nanoparticle. Zooming out of the region of analysis shown in Figure 1 exposes hundreds of plasmonic nanoparticles in the field of view, see Figure 2. As such, the same analysis carried

out on the isolated plasmonic silver nanoparticle can be repeated for hundreds of individual scatterers in our field of view in parallel (analysis will be detailed elsewhere¹²). Not surprisingly,^{10,11,14} we observe marked differences between the optical signatures of the different isolated particles in terms of (i) their relative scattering efficiencies, (ii) their resonance maxima, and (iii) their derived peak widths which can be used to derive the plasmon dephasing time of each of the particles in our field of view.¹² Evidently, the spatial resolution obtained using this diffraction-limited optical technique is not sufficient to examine the nanometric structural specifics which govern the optical response of each particle, a concept eluded to in prior works^{10,11,14} and further bolstered in the following sections. Correlating the recorded spectral images with topographic scanning/transmission electron micrographs is one option. Beyond resorting to correlated topographical and optical measurements,^{10,11,14} the need for techniques that can be used to map SPs on much finer length scales presents itself in this context.

Simultaneous Topographic and Local Electric Field Imaging *via* Frequency-Resolved TERS

We recently reported frequency-resolved TERS imaging measurements in which a Raman-active 4,4'-dimercaptostilbene (DMS)-coated gold tip of an atomic force microscope was employed to simultaneously (i) map the topography, and (ii) image the LSP-enhanced electric fields sustained in the vicinity of nanometric slits (20 and 5 nm-wide) lithographically etched in a silver thin film, see Figure 3A.¹⁵ Bi-modal imaging is feasible by virtue of the nature of the optical response of the chemically functionalized metal probe. Namely, the probe

position-dependent optical signal can be sub-divided into two components, see Figure 3A. The first is a 500-2250 cm⁻¹ Stokes-shifted signal, characteristic of the tip-bound DMS molecules. The molecular signal reports on topography through the intensity contrast observed as the tip is scanned across the lithographic patterned ultrafine slits, see Figure 3B. The variation in molecular TERS activity is a consequence of the absence/formation of a plasmonic junction between the scanning probe and patterned silver surface, which translates into dimmed/enhanced Raman signatures of DMS. Using these signals, we experimentally demonstrated that sub-15 nm (topographic) spatial resolution is attainable using a DMS-coated gold tip with a 30 nm radius, see Figure 3B.¹⁵ The second optical response consisted of two correlated sub-500 cm⁻¹ signals arising from mirror-like reflections of (i) the incident laser field, and (ii) the Raman scattered response of an underlying glass support (at 100-500 cm⁻¹) off the gold tip. We demonstrated that the reflected signals trace the local electric fields in the vicinity of the nanometric slits, see Figure 3C. We found that the recorded local electric field maps are convoluted with the full tip radius.¹⁵ Although this limits the attainable spatial resolution to the tens of nanometers length scale, the spatial resolution demonstrated in our recent work is at least an order of magnitude finer than the diffraction limit of light.¹⁵ That said, as molecular Raman spectra are simultaneously recorded at every tip position, this approach is potentially much more informative, particularly if it were to be extended to the single molecule regime.^{1,16} For instance, by taking advantage of the tensorial nature of single molecule Raman scattering, it may be possible to image the vector components of the localized electric fields across a plasmonic substrate.¹⁶ In the same vein, the absolute magnitude of the local electric field can also be gauged from vibrational Stark shifts, previously observed in TERS from molecular

reporters coaxed into plasmonic tip-sample nanojunctions.¹⁶ Cross-checking the insights gained from the aforementioned molecular scattering measurements would require independent access to the immediate local environment (electric fields) of a single molecule. This motivates the following sections, where plasmonic fields are imaged at the ultimate space-time and space-energy limits.

Imaging Localized and Propagating Surface Plasmons with Nonlinear Photoemission Electron Microscopy

A photoemission electron microscope powered by a femtosecond laser source is a powerful tool that can be used to image both LSP-enhanced electric fields in plasmonic nanoparticles^{14,17} as well as PSPs launched on metallic surfaces using lithographically patterned coupling structures,^{9,18} with a spatial resolution on the order of ten nanometers. We recently employed time-integrated nonlinear photoemission electron microscopy (PEEM) to map the LSP-enhanced electromagnetic fields in the vicinity of plasmonic silver nanoparticles supported on a silver thin film.¹⁴ Under 400 nm fs laser irradiation, a two-photon excitation process is required to exceed the work function of silver (~4.2 eV¹⁹). The photoelectron yield is thus proportional to the square of the laser intensity, or the fourth power of the local electric field. When normalized to the two-photon PEEM image of a reference, such as a nominally flat silver film, LSP-enhanced electromagnetic fields can be directly visualized.¹⁴ Figure 4 shows correlated two-photon PEEM and scanning electron microscopy (SEM) images of an isolated silver nanoparticle supported on a silver thin film. The two-photon PEEM enhancement images recorded following p- and s-polarized 400-nm femtosecond laser irradiation are shown in

Figures 4A and 4B, respectively. Notice how the latter image is reminiscent of the dipolar plasmon resonance of an isolated silver nanosphere. That said, the inequivalent enhancement factors and dissimilar spatial profiles of the upper and lower lobes are noted. These differences can be rationalized on the basis of the SEM image of the same particle shown in Figure 4C; the particle is slightly oblong and features nanometric irregularities that are (faintly) visible in its SEM image. Of some 27 particles featuring comparable diameters that were analyzed in the original report,¹⁴ only 16 exhibited a dipolar pattern similar to the one shown in Figure 4B. The remaining 11 particles featured irregular photoemission patterns that were traced back to their unique nanometric structural specifics, as evidenced from correlated SEM imaging experiments.¹⁴ The main conclusion of this work is that nanometric structural defects that are often finer than the typical resolution afforded by SEM govern the recorded non-linear PEEM images, and hence, the 2D profiles of the LSP-enhanced electric fields. As illustrated in the next sub-section, finer spatial resolution can be obtained using electron energy loss spectroscopy (EELS).

In the above-described multi-photon PEEM scheme, photoemission is induced by a nonlinear process. By splitting the driving femtosecond laser source into two equal parts and subsequently recombining the resulting two femtosecond pulses in an interferometer, it is possible to record time-resolved nonlinear PEEM (tr-PEEM)^{9,18} images in a pump-probe fashion. We recently employed tr-PEEM to image PSPs launched from a patterned rectangular trench lithographically milled into flat gold surface. Notably, joint nanometer spatial and sub-femtosecond temporal resolution was achieved in our prior work.⁹ Our tr-PEEM scheme involved a pair of identical, spatially offset, and interferometrically-locked femtosecond laser

pulses, termed ‘pump’ and ‘probe’ pulses from hereon. Figure 5A shows a PEEM image recorded following combined pump and probe excitation. The spatially offset probe pulse is temporally delayed by approximately 43.3 fs with respect to the pump pulse, such that it arrives at the gold surface at the same time as the PSP generated by the pump pulse at the trench position.⁸ Photoemission from the polarization state prepared by the probe pulse and the PSP wave packet is clearly observable in the upper right region of Figure 5A. This demonstrates that the PSP wave packet propagates at least 150 μm from its original launching point, namely the trench coupling structure illustrated in the lower left of Figure 5A, without significant dephasing. The 2D spatial profile of the imaged PSP is affected by (i) the elliptical profiles of the laser spots, incident onto the sample surface at a low angle of incidence, (ii) the profile of the launched PSP, (iii) convolution with pump and probe pulses, and (iv) interference with PSP waves packets launched from the upper and lower corners of the trench.⁹ The last effect is most evident in the first interference fringe closest to the trench, where a double-lobed pattern and a nodal plane are clearly visible, see Figure 5A. Figure 5B shows photoemission intensity as function of pump-probe time delay, at a position located 135 μm away from the plasmonic coupling structure. The two Gaussian fits of the field envelope indicate the time when the probe pulse interferes with the pump (blue) and PSP wave packet (green).⁹ Using these intererometric time traces, we were able to directly measure various properties of the surface-bound wave packet, including its carrier wavelength (783 nm) and group velocity (0.95c).

Imaging Surface Plasmons with Electron Energy Loss Spectroscopy

SP resonances are sensitive to nanometric structural variations in metal nanostructures; an observation alluded to in the previous sections. By virtue of its flexibility, the (scanning) transmission electron microscope ((S)TEM) has become the instrument of choice for the structural and chemical characterization of metal clusters and nanoparticles, with high spatial resolution.²⁰ Using the electron beam in a STEM setup equipped with an electron energy loss (EEL) spectrometer, energy-resolved maps of the enhanced electric fields associated with SPs can be recorded.²¹ In STEM, the local varying electric field produced by an incident fast electron (typically 60-300kV) polarizes a metal nanostructure as it passes near or through it. The characteristic resonant oscillations (plasmons) in turn generate induced local electric fields that act back on the moving electrons.²² The signal detected by the EEL spectrometer is the energy loss suffered by the individual beam electrons due to the force exerted by the induced local electric field. EEL spectra can be recorded from selected locations around a nanoparticle, or can be acquired in a serial fashion by scanning the probe across an area of interest pixel by pixel; producing what is essentially a hyperspectral (energy resolved) image. In this fashion, the spatial distribution of the induced electric fields can be mapped.²³ Using spherical aberration-corrected microscopes, it is now possible to produce intense electron probes 1 Ångström or smaller in diameter; the ultimate spatial resolution achieved using this technique is of utmost importance to the fields of ultrasensitive chemical detection and imaging. In addition, electron monochromators can be used to reduce the energy spread of the electron beam to achieve energy resolutions as low as <10 meV,²⁴ *vide infra*. For extended reviews on EELS (and of cathodoluminescence in STEM) applications in plasmonics, the reader is referred to the works of Garcia de Abajo as well as Kociak and Stéphan.²¹

The ability to spatially resolve highly localized plasmon resonances using STEM-EELS has provided experimental evidence for the size and shape dependence of the LSP response of individual particles,^{21,25} the excitation of multipole modes in larger particles,²⁶ and the hybridized plasmonic response of interacting plasmonic nanoparticles,^{23,24,27} to name a few applications. EELS can also provide valuable information about current-carrying quantum plasmons, namely charge transfer plasmons,²⁸ and ultrasmall plasmonic nanoparticles.²⁹ The length scales of relevance to this problem are on the order of/less than 1 nm. As such, EELS is one of the few techniques that can be used to directly address charge-shuttling quantum plasmons. Additional advantages of using STEM-EELS to probe the plasmonic response of sub-wavelength metal nanoparticles include: (i) the technique's ability to provide information from the interior of the sample as signals are collected in transmission, (ii) the possibility of manipulating interparticle distances with the electron beam,²⁶ and (iii) the possibility to take advantage of the many analytical capabilities (imaging, diffraction, chemical characterization by EEL and energy-dispersive X-ray spectroscopies) that are available in a STEM instrument.

As an exemplary demonstration of STEM-EELS, we discuss measurements targeting a single-crystal {100}-facetted Ag nanobar (aspect ratio ~3.5) supported on a 5 nm amorphous Si layer, see Figure 6. It is important to note that although similar structures have been investigated in prior EELS studies, using the current monochromated system allows us to obtain much higher signal-to-noise ratios and to continuously vary our energy resolution. Hyperspectral EELS maps and high angle annular dark field (HAADF) images of the Ag nanobar were acquired using a Cs-corrected and monochromated Nion UltraSTEM 100MC ('Hermes') microscope operated at 60kV and equipped with a Gatan Enfinium ERS spectrometer. The

resolution (full-width at half-maximum of the zero-loss peak) was 40meV for the results in Figure 6, 7A, 7B and 7F and 16meV for the data shown in Figures 7D and 7E. The probe size for the 40meV data was smaller than 1.4 Å; the {220} Ag planes were resolved in our experiments. The HAADF image shown in Figure 6A illustrates the projected geometry of the structure probed using hyperspectral EELS, namely, the Ag nanobar structure. The contrast in such images is to a good approximation proportional to the atomic number of the material as $\sim Z^{1.7}$ and to local thickness, such that the nano-bar appears bright, surrounded by dim grey areas corresponding to the ultrathin Si support. An average EEL spectrum obtained by summing over all the individual EEL spectra collected within the highlighted area of interest is shown in Figure 6B. Two main plasmon resonances are visible at 1.45 eV and 3.45 eV, corresponding to the two characteristic LSP resonances of the rod along its long (longitudinal) and short (transverse) axes, respectively.³⁰ The narrower peak at 3.85 eV corresponds to the bulk plasmon of the structure. The corresponding numerical simulations shown in Figures 6D and 6E were performed using the finite-element method (FEM), as implemented in a commercially available software package (COMSOL Multiphysics v5.2). The simulated construct includes the nanobar and the underlying 5nm-thick amorphous Si substrate; the geometry and dimensions used in the simulation closely resemble their experimental analogues (see the inset of Figure 6E). As shown in Figure 6E, the longitudinal and transverse plasmon modes are apparent in the simulations for the parallel (longitudinal) and horizontal (transverse) incident polarizations, respectively, and the simulated values are in good agreement with their experimental analogues.

The enhanced electric fields associated with SP eigenmodes can be directly visualized using EELS, see Figures 6C. For instance, the familiar dipolar response of the rod in the 1.4-

1.5eV energy range is clearly distinguishable from its quadrupole (anti-symmetric) resonance in the 2.1-2.2eV energy range. Note that the wavenumbers of the resonances measured are large. This is a result of the relatively small length of the nanowire used herein. The wavenumbers can be conveniently derived from our EELS data as $k_p=\pi/(2d_{EELS})$, where d_{EELS} is the distance between intensity maxima.³¹ As such, lower order modes begin to converge towards the plasmonic response of an extended planar surface.^{31,32} As shown in Figure 6C, we spatially resolve the planar surface plasmon in the 3.4-3.5eV energy range.

More recently, the use of electron energy monochromators has enabled the detection of LSPs in the infrared spectral region, namely, below 1eV.³¹ By taking advantage of the improved energy resolution, EELS can be potentially used as a quantitative tool, for instance, to gauge damping effects in single particles and/or to measure the electron kinetics of single plasmonic modes³³. Prerequisite to achieving quantitative LSP analysis is attaining an experimental energy resolution that is finer than the natural line width of the plasmon resonance of interest. In Figure 7, we illustrate the effect of energy resolution (and signal-to-noise) ratio on EELS observables, by examining the spectra collected at proximal locations on/around the nanobar using different microscope settings (integrated over a four times larger area at the lower energy resolution). Figure 7A and 7D display the zero-loss EELS peaks comparing the 40 and 16 meV resolution obtained in Figures 7B and 7E, respectively. The locations at which the spectra were acquired – both through (position 4) and in the vicinity of the nanobar (positions 1-3) – are highlighted in Figure 7C. Whilst resolving faster processes would require higher energy resolution, in this particular example, we note that the measured width of the narrowest feature probed, i.e. the bulk plasmon mode, is unaffected by the

nominal instrument resolution, as indicated by the dotted lines sketched in Figures 7B and 7E.

As such, an energy resolution of 40meV appears to be narrower than the natural line width of this (bulk) plasmon resonance. An increased energy resolution at the cost of a smaller signal-to-noise ratio is therefore not required in this particular example.

Brief Conclusions and Outlook

Through select practical examples from our own laboratories, we demonstrated how localized and propagating surface plasmons can be visualized over the length (down to atomic resolution) and time (at a sub-femtosecond time resolution) scales dictated by their nanoscopic and dissipative nature. We reviewed recent works from our own groups which take advantage of various techniques powered by photons, photoelectrons, and electrons. Hyperspectral optical micrographs are inherently diffraction limited. Nonetheless, the simplicity of our recently developed scattering micro-spectroscopy capability, which can be trivially incorporated into a surface/tip-enhanced Raman nano-spectroscopy setup is attractive. On the other hand, non-linear photoemission electron microscopy affords joint nanometer-sub-fs resolution, which is ideal to follow surface plasmons propagating on the surface of a nanostructured plasmonic metal. Single particle spectral images (optical) and local electric field maps (PEEM) both suggest that each plasmonic nanoparticle has its own unique character. This motivates the use of hyperspectral EELS microscopy, where the ultimate spatial resolution is achieved in local electric field imaging.

In the realm of electron microscopy, we note that there is much more to hyperspectral EELS than visualizing the local electric fields associated with SP excitation. For instance,

estimations of the decay lengths of the evanescence fields can also be made using this technique.³¹ That said, the relationship between the local electric field strength and electron energy loss continues to be a subject of debate.³⁴ A quantitative analysis of EELS maps, such as the one shown in Figure 7F, which shows the longitudinal dipole mode recorded at a low magnification, could ultimately answer outstanding questions such as (i) how do SP localized on adjacent plasmonic nanostructures interact/hybridize, and (ii) how far do LSP fields extend? Answering both questions is particularly valuable for surface- and tip-enhanced Raman scattering measurements specifically, and the field of plasmonic sensing more broadly. Dephasing times may also be reliably estimated from EELS maps obtained at high spectral resolution, where the equivalent of a temporal resolution of 1 fs is achieved with a 16 meV energy resolution at 3.95eV, see Figures 7D and 7E. At this resolution, the vibrational signatures from a range of materials²⁴ has been measured, and the derived vibrational signatures were correlated with molecular infrared spectra.³⁵ Although many organic materials are sensitive to electron beam induced radiation damage, organic molecules can be preserved by performing EELS using the so-called aloof-beam mode, where the electron beam is placed at a distance from the area of interest;³⁶ this provides sufficient signal-to-noise for vibrational EEL spectroscopy, all while retaining a degree of spatial localisation.²⁴ We finally note that the prospect of characterizing either bare or chemically functionalized plasmonic nanostructures at the ultimate limits of space and time through a combination of all of the aforementioned tools is a most exciting prospect and goal that we hope to achieve in the near future.

Acknowledgments

We concede that the scope of this mini-review is biased towards techniques employed/works performed by our own groups; this mini-review is not comprehensive in nature. PZE was supported by the Laboratory Directed Research and Development Program through a Linus Pauling Fellowship at Pacific Northwest National Laboratory (PNNL), and acknowledges an allocation of computing time from the National Science Foundation (TG-CHE130003). YG, AGJ, and WPH were supported support by the US Department of Energy (DOE), Office of Science, Office of Basic Energy Sciences, Division of Chemical Sciences, Geosciences & Biosciences. A portion of the work was performed using EMSL, a national scientific user facility sponsored by the DOE's Office of Biological and Environmental Research and located at PNNL. PNNL is a multiprogram national laboratory operated for DOE by Battelle. EELS measurements were performed at SuperSTEM, the U.K. National Facility for Aberration-Corrected STEM, supported by the Engineering and Physical Sciences Research Council (PA, FSH, and QMR).

FIGURES

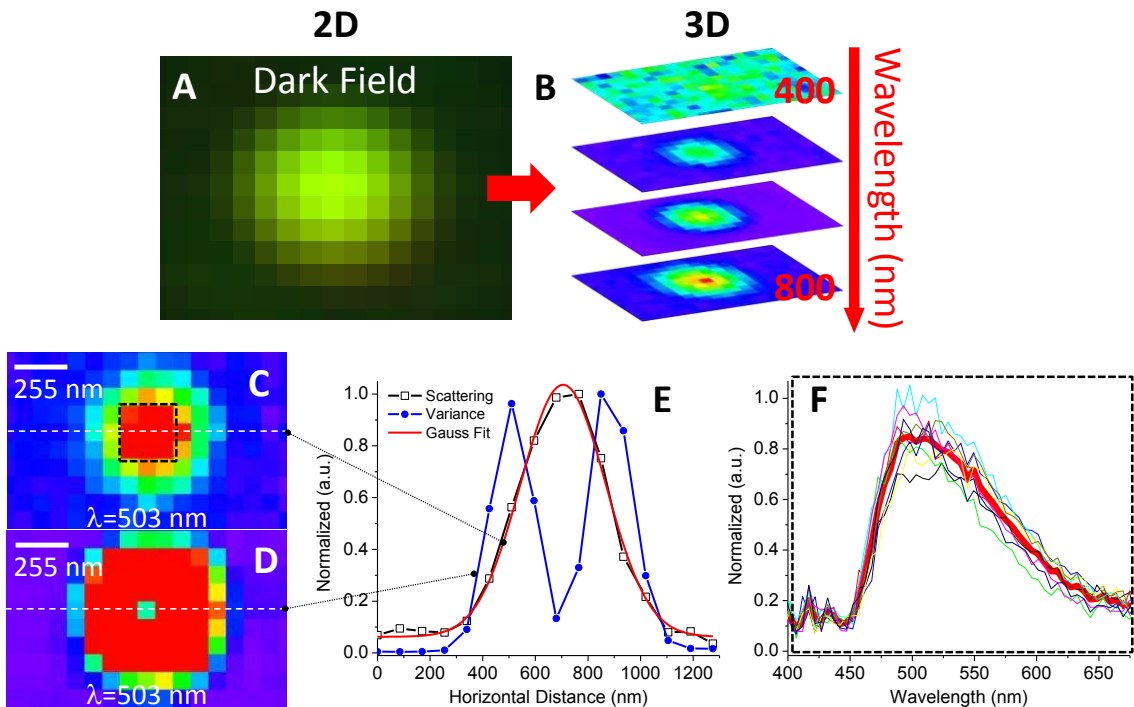


Figure 1. A) Real color image of the scattering from an isolated silver nanoparticle (diameter = 100 nm) on glass. B) Schematic illustration of the information content in hyperspectral dark field scattering optical microscopy. C) Single particle scattering image at 503 nm, which after applying a variance filter based on a co-occurrence matrix (3x3 pixel window) yields the image shown in panel D. E) Horizontal cross-sections taken from panels C and D. Also shown in this panel is a Gaussian fit to the scattering cross-section taken from panel C. F) 9 dark field scattering spectra extracted from individual pixels contained in the 3x3 pixel area highlighted using a dashed square in panel C. The thick red line represents the average of all nine spectra.

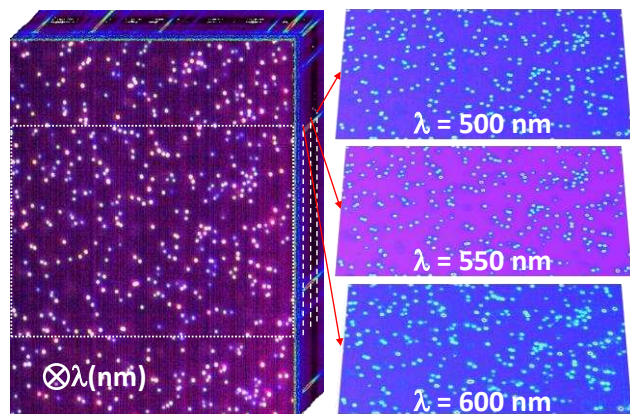


Figure 2. 3D representation of a hyperspectral dark field image of 100 nm silver nanospheres dispersed on a glass microscope slide is shown in the left panel. The field of view in this panel is $\sim 44 \times 59 \mu\text{m}^2$. Images slices, namely dark field optical images recorded at different wavelengths, are stacked in the right panel.

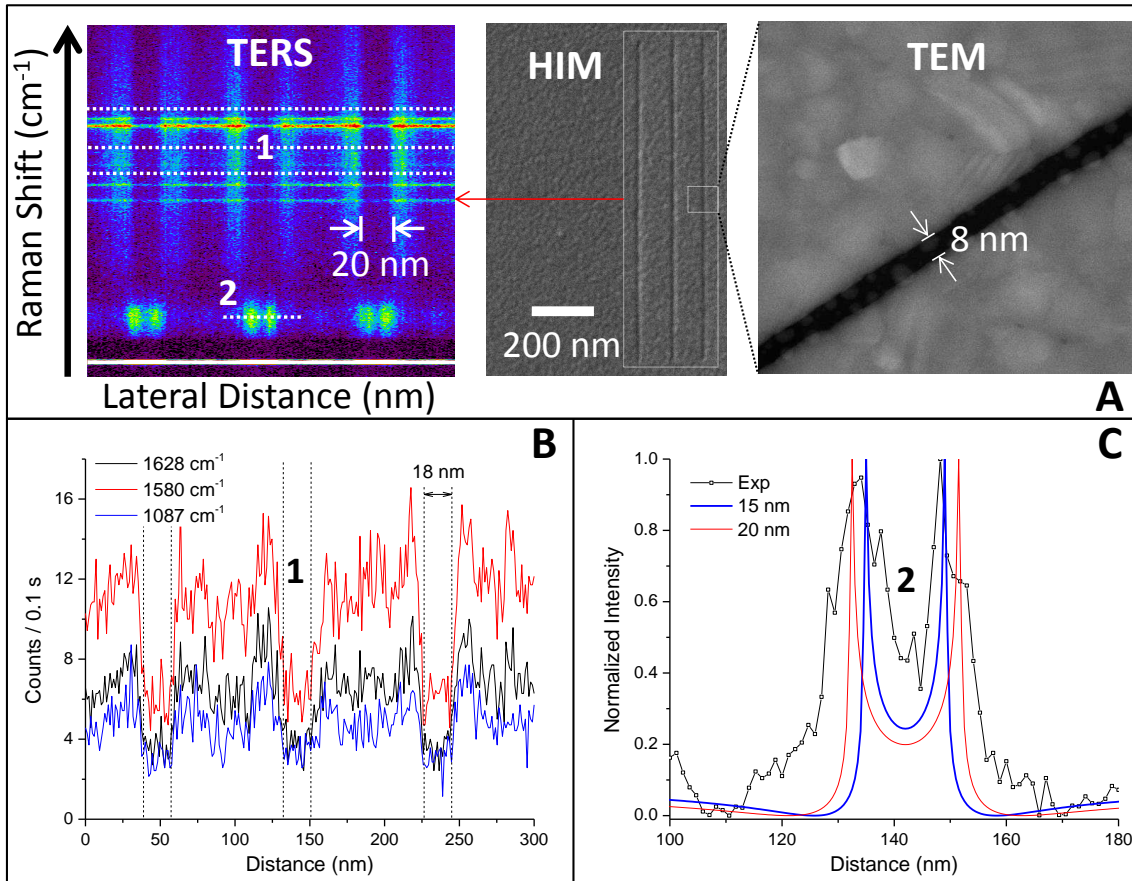


Figure 3. A) Left panel: Hyperspectral TERS cross-section of three adjacent 20 nm wide slits lithographically etched in a silver thin film using helium ion lithography. Middle panel: Helium ion microscopy image of the three milled slits. Right panel: Selected area TEM image illustrating that well-defined sub-10 nm slits with rather sharp edges can be fashioned using helium ion lithography. B) The recorded intensities at 1628, 1580, and 1087 cm^{-1} (molecular signals) as the AFM tip is scanned across the three slits. C) A reflected low-frequency signal is compared to the finite-difference time domain- (FDTD, *Lumerical FDTD Solutions*) simulated local electric fields (E_{total}/E_0) sustained near isolated 15 and 20-nm wide slits following focused (40 X objective, 0.7 NA) 514 nm irradiation. Note that the FDTD simulations assume perfect surface and slit structures. The reader is referred to reference [15] for more specifics.

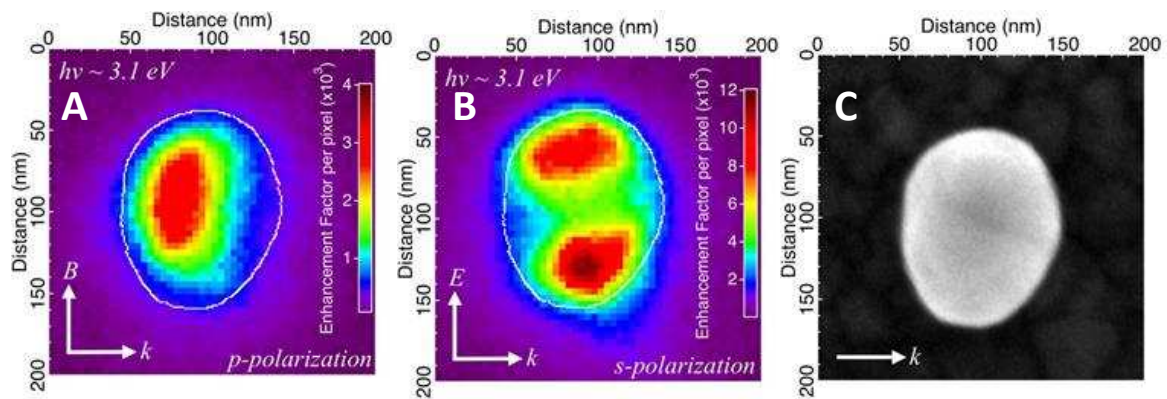


Figure 4. A) High magnification ($\times 10^5$) multi-photon PEEM image of a 114 nm diameter silver nanoparticle supported on a silver thin film. The sample is illuminated by p-polarized, 400 nm fs laser pulses at an incidence angle of 75° . B) PEEM image recorded following s-polarized laser irradiation. The field of view in Panel A is preserved. C) Correlated SEM image of the silver nanoparticle imaged in Panels A and B. Note that the relative orientation of the nanoparticle on the surface is preserved throughout all three Panels. An outline of the nanoparticle derived from the SEM image is overlaid in Panels A and B.

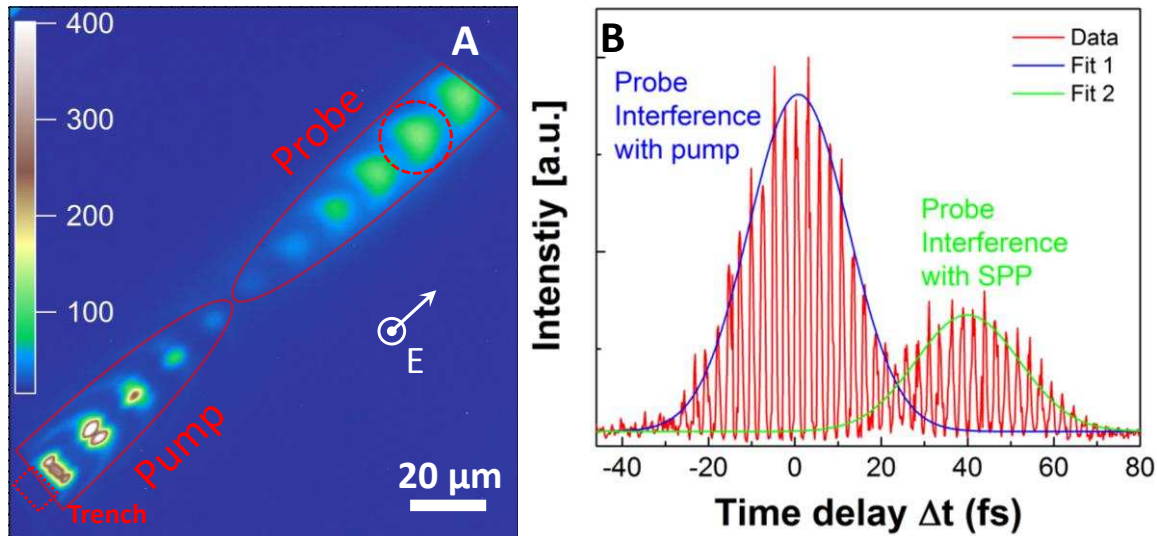


Figure 5. A) PEEM image of a photoemission interference pattern, observed when both the pump and probe pulse are incident onto the sample, but are spatially separated. The pump is incident onto a trench (red dashed squares in the lower left) lithographically etched in a nominally flat gold thin film. The probe is centered towards the upper right corner of the image, as schematically illustrated. The pattern observed at the probe beam position is a result of the interference between the probe beam and the PSP wave packet launched from the trench by the spatially separated pump beam. Both pump and probe pulses are polarized with an electric vector parallel to the out-of-plane axis (p-polarized). B) Interferometric photoemission intensity as function of pump-probe delay time, at a position 135 μm from the plasmonic trench, designated by a dashed red circle in panel A. The two Gaussian fits of the field envelope designate the time delays at which the probe pulse interferes with pump (blue, $t=0$) and PSP wave packet (green, $\Delta t = 43.3$ fs). The reader is referred to reference [9] for more specifics.

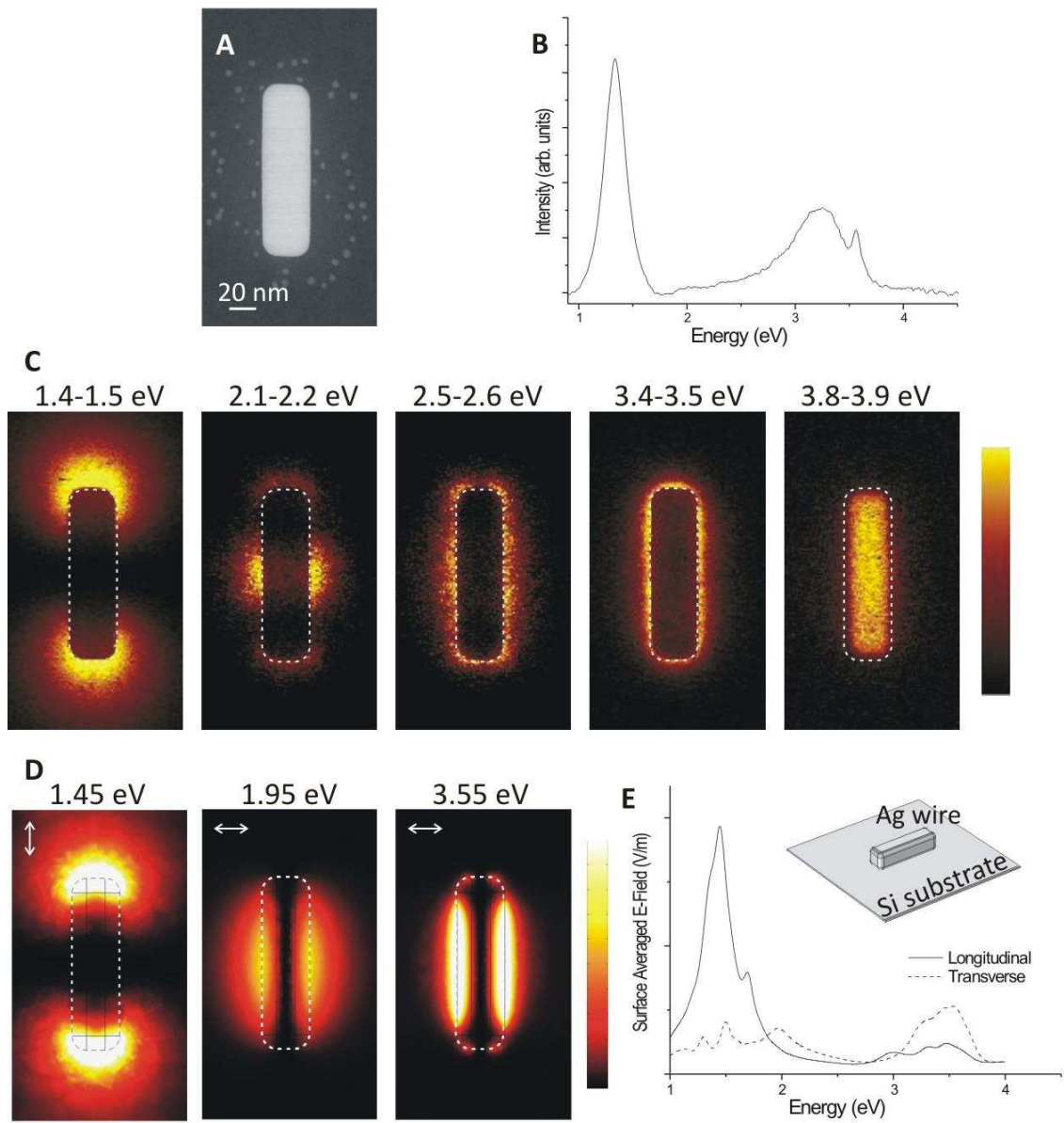


Figure 6. A) Dark-field (Z-contrast) image of a silver nanobar (length x width= 129 nm x 36 nm, AR \approx 3.5) supported on a 5nm thick amorphous silicon substrate. The additional bright dots that are noticeable on the substrate are attributed to impurities in the colloidal suspension used to prepare the sample. B) EELS spectrum obtained by averaging the spectra in each pixel comprising the EELS map taken in area A (total = 100 x 181 pixels). C) STEM-EELS maps at the designated energy ranges. The experimental maps are normalized to the maximum intensity in

each case. D) Calculated z-component of the electric field, $|E_z|^2$, following vertically polarized (left) and horizontally polarized optical irradiation (middle and right). The intensity scale for the simulated maps is the same for all, except for the 1.95eV, which has been multiplied by 2. E) Averaged electric field map obtained by summing the magnitudes computed for each of the aforementioned incident polarizations. The inset shows a perspective view of the simulated construct comprising a 36 nm x 129 nm nanobar supported on a 5nm thick Si substrate.

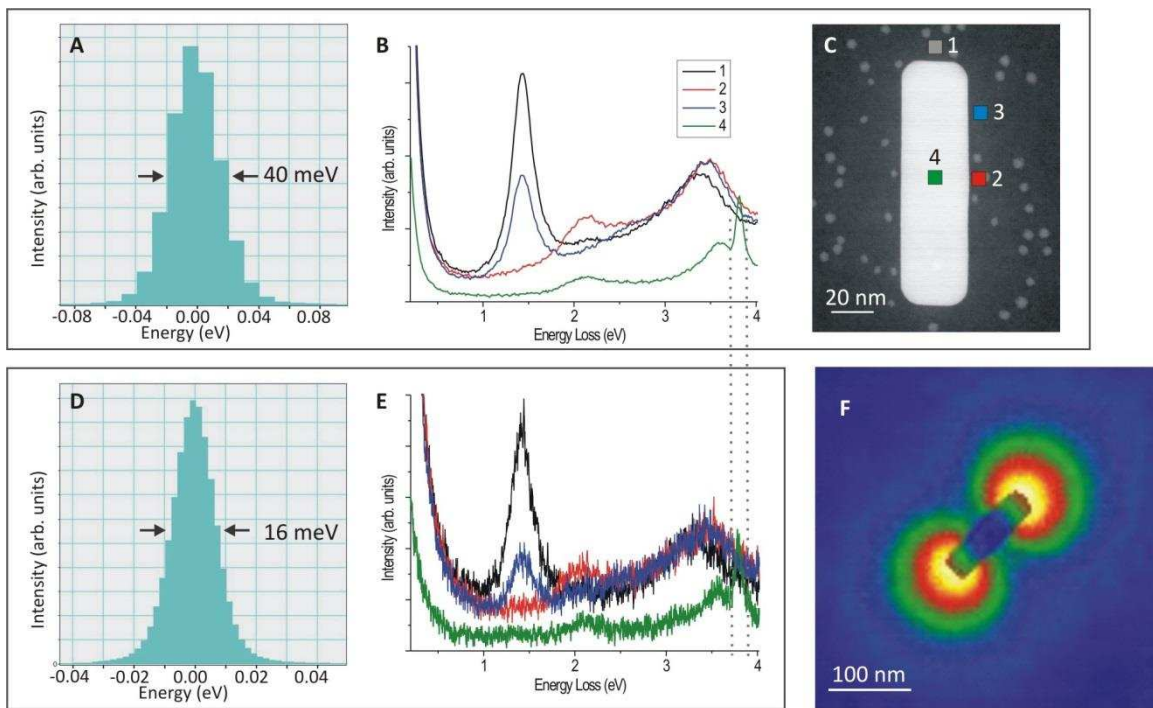


Figure 7. A) Zero-loss EELS peak obtained by averaging the spectra in a ~4nm x 4nm area, which is comparable to the areas used for spectral averaging (averaged spectra shown in B) at locations 1-4 (designated in C). D-E are similar to A-B, but in this case an ~8nm x 8 nm area is used to get the zero-loss EELS peak and the spatially averaged spectra in the same vicinity (locations 1-4 in C). F) EELS map at 1.45eV, in which the longitudinal dipolar LSP mode can be observed at low magnification (spectral image of 100 x 100 pixels size and 0.01 eV dispersion).

References

-
- ¹ E. Le Ru and P. G. Etchegoin, *Annu. Rev. Phys. Chem.*, 2012, **63**, 65; S. Nie and S. R. Emory, *Science*, 1997, **275**, 1102; K. Kneipp, Y. Wang, H. Kneipp, L. Perelman, I. Itzkan, R. Dasari and M. Feld, *Phys. Rev. Lett.*, 1997, **78**, 1667; P. Z. El-Khoury, G. E. Johnson, I. V. Novikova, Y. Gong, A. G. Joly, J. E. Evans, M. Zamkov, J. Laskin and W. P. Hess, *Faraday Discuss.*, 2015, **184**, 339.
- ² J. Steidtner and B. Pettinger, *Phys. Rev. Lett.*, 2008, **100**, 236101; R. Zhang, Y. Zhang, Z. C. Dong, S. Jiang, C. Zhang, L. G. Chen, L. Zhang, Y. Liao, J. Aizpurua, Y. Luo et al., *Nature*, 2013, **498**, 82; M. D. Sonntag, J. M. Klingsporn, L. K. Garibay, J. M. Roberts, J. A. Dieringer, T. Seideman, K. A. Scheidt, L. Jensen, G. C. Schatz and R. P. Van Duyne, *J. Phys. Chem. C*, 2012, **116**, 478.
- ³ M. L. Brongersma, N. J. Halas and P. Nordlander, *Nature Nanotech.*, 2015, **10**, 25.
- ⁴ S. Yampolsky, D. A. Fishman, S. Dey, E. Hulkko, M. Banik, E. O. Potma and V. A. Apkarian, *Nat. Photonics.*, 2014, **8**, 650.
- ⁵ T. W. Ebbesen, C. Genet and S. I. Bozhevolnyi, *Phys. Today*, 2008, **61**, 44.
- ⁶ J. M. Pitärke, V. M. Silkin, E. V. Chulkov and P. M. Echenique, *Rep. Prog. Phys.*, 2007, **70**, 1.
- ⁷ W. L. Barnes, A. Dereux and T. W. Ebbesen, *Nature*, 2003, **424**, 824; L. Yin, V. K. Vlasko-Vlasov, A. Rydh, J. Pearson, U. Welp, S. H. Chang, S. K. Gray, G. C. Schatz, D. B. Brown and C. W. Kimball, *Appl. Phys. Lett.*, 2004, **85**, 467; K. G. Lee and Q. H. Park, *Phys. Rev. Lett.*, 2005, **95**, 103902.
- ⁸ Z. Liu, J. M. Steele, W. Srituravanich, Y. Pikus, C. Sun and X. Zhang, *Nano. Lett.*, 2005, **5**, 1726; L. Verslegers, P. B. Catrysse, Z. F. Yu, J. S. White, E. S. Barnard, M. L. Brongersma and S. H. Fan, *Nano. Lett.*, 2009, **9**, 235; L. Lin, X. M. Goh, L. P. McGuinness and A. Roberts, *Nano. Lett.*, 2010, **10**, 1936.
- ⁹ Y. Gong, A. G. Joly, D. Hu, P. Z. El-Khoury and W. P. Hess, *Nano Lett.*, 2015, **15**, 3472.
- ¹⁰ E. Ringe, B. Sharma, A. Henry, L. D. Marks and R. P. Van Duyne, *Phys. Chem. Chem. Phys.*, 2013, **15**, 4110; A. I. Henry, J. M. Bingham, E. Ringe, L. D. Marks, G. C. Schatz and R. P. Van Duyne, *J. Phys. Chem. C*, 2011, **115**, 9291.
- ¹¹ K. Lindfors, T. Kalkbrenner, P. Stoller and V. Sandoghdar, *Phys. Rev. Lett.*, 2004, **93**, 037401; C. Novo, D. Gomez, J. Perez-Juste, Z. Zhang, H. Petrova, M. Reismann, P. Mulvaney and G. V. Hartland, *Phys. Chem. Chem. Phys.*, 2006, **8**, 3540; A. Tcherniak, J. W. Ha, S. Dominguez-Medina, L. S. Slaughter and S. Link, *Nano Lett.*, 2010, **10**, 1398. N. Fairbairn, A. Christofidou, A. G. Kanaras, T. A. Newman and O. L. Muskens, *Phys. Chem. Chem. Phys.*, 2013, **15**, 4163.
- ¹² P. Z. El-Khoury, A. G. Joly and W. P. Hess, submitted.
- ¹³ R. M. Haralick, K. Shanmugam and I. Dinstein, *IEEE Transactions on Systems, Man, and Cybernetics*, 1973, **SMC-3**, 610.
- ¹⁴ S. J. Peppernick, A. G. Joly, K. M. Beck and W. P. Hess, *J. Chem. Phys.*, 2013, **138**, 154701.
- ¹⁵ P. Z. El-Khoury, Y. Gong, P. Abellán, B. W. Arey, A. G. Joly, D. H. Hu, J. E. Evans, N. D. Browning and W. P. Hess, *Nano. Lett.*, 2015, **15**, 2385.
- ¹⁶ M. Banik, P. Z. El-Khoury, A. Nag, A. Rodriguez-Perez, N. Guarrotxena, G. C. Bazan and V. A. Apkarian, *ACS. Nano*, 2012, **6**, 10343; J. M. Marr and Z. D. Schultz, *J. Phys. Chem. Lett.*, 2013, **4** (2013), 3268; D. T. Kwasnieski, H. Wang and Z. D. Schultz, *Chem. Sci.*, 2015, **6**, 4484; P. Z. El-Khoury, P. Abellán, R. L. Chantry, Y. Gong, A. G. Joly, I. V. Novikova, J. E. Evans, E. Aprà, D. Hu, Q. M. Ramasse and W. P. Hess, *Adv. Phys.: X*, 2016, DOI: 10.1080/23746149.2016.1140010.

-
- ¹⁷ M. Cinchetti, A. Gloskovskii, S. A. Nepjiko, G. Schönhense, H. Rochholz and M. Kreiter, *Phys. Rev. Lett.*, 2005, **95**, 047601; C. Hrelescu, T. K. Sau, A. L. Rogach, F. Jäckel, G. Laurent, L. Douillard and F. Charra, *Nano Lett.*, 2011, **11**, 402; P. Melchior, D. Bayer, C. Schneider, A. Fischer, M. Rohmer, W. Pfeiffer and M. Aeschlimann, *Phys. Rev. B*, 2011, **83**, 235407; F. Schertz, M. Schmelzeisen, R. Mohammadi, M. Kreiter, H. -J. Elmers, and G. Schönhense, *Nano Lett.*, 2012, **12**, 1885.
- ¹⁸ A. Kubo, K. Onda, H. Petek, Z. J. Sun, Y. S. Jung, and H. K. Kim, *Nano Lett.*, 2005, **5**, 1123; L. M. Wang, L. X. Zhang, T. Siedeman, and H. Petek, *Phys. Rev. B*, 2012, **86**, 165408.
- ¹⁹ M. Chelvayohan and C. H. B. Mee, *J. Phys. C*, 1982, **15**, 2305.
- ²⁰ M. Vollmer and U. Kreibig, Optical Properties of Metal Clusters, Springer Series in Materials Science Vol. 25, 1995.
- ²¹ F. G. De Abajo, *Rev. Mod. Phys.*, 2010, **82**, 209; M. Kociak and O. Stéphan, *Chem. Soc. Rev.*, 2014, **43**, 3865.
- ²² R. F. Egerton, *Electron Energy-Loss Spectroscopy in the Electron Microscope*, Springer, New York, 3rd edn., 2011.
- ²³ J. Nelayah, M. Kociak, O. Stéphan, F. J. G. de Abajo, M. Tencé, L. Henrard, D. Taverna, I. Pastoriza-Santos, L. M. Liz-Marzán and C. Colliex, *Nat. Phys.*, 2007, **3**, 348.
- ²⁴ O. L. Krivanek, T. C. Lovejoy, N. Dellby, T. Aoki, R. Carpenter, P. Rez, E. Soignard, J. Zhu, P. E. Batson and M. J. Lagos, *Nature*, 2014, **514**, 209; R. Brydson, *Nature*, 2014, **514**, 177; P. Rez, *Microsc. Microanal.*, 2014, **20**, 671; R. Egerton, *Ultramicroscopy*, 2015, **159**, 95; R. Nicholls, F. Hage, J. Yates, D. McCulloch, D. Kepartsoglou, T. Lovejoy, N. Dellby, O. Krivanek, K. Refson and Q. Ramasse, *Microsc. Microanal.*, 2015, **21**, 1469.
- ²⁵ M. Bosman, V. J. Keast, M. Watanabe, A. I. Maaroof and M. B. Cortie, *Nanotechnology*, 2007, **18**, 165505; M. N'Gom, S. Li, G. Schatz, R. Erni, A. Agarwal, N. Kotov and T. B. Norris, *Phys. Rev. B*, 2009, **80**, 113411; S. Mazzucco, N. Gequet, J. Ye, O. Stéphan, W. Van Roy, P. Van Dorpe, L. Henrard and M. Kociak, *Nano Lett.*, 2012, **12**, 1288; M. J. McClain, A. E. Schlather, E. Ringe, N. S. King, L. Liu, A. Manjavacas, M. W. Knight, I. Kumar, K. H. Whitmire and H. O. Everitt, *Nano Lett.*, 2015, **15**, 2751.
- ²⁶ I. Alber, W. Sigle, F. Demming-Janssen, R. Neumann, C. Trautmann, P. A. van Aken and M. E. Toimil-Molares, *ACS Nano*, 2012, **6**, 9711; B. S. Guiton, V. Iberi, S. Li, D. N. Leonard, C. M. Parish, P. G. Kotula, M. Varela, G. C. Schatz, S. J. Pennycook and J. P. Camden, *Nano Lett.*, 2011, **11**, 3482; M.-W. Chu, V. Myroshnychenko, C. H. Chen, J.-P. Deng, C.-Y. Mou and F. J. García de Abajo, *Nano Lett.*, 2008, **9**, 399.
- ²⁷ A. L. Koh, A. I. Fernández-Domínguez, D. W. McComb, S. A. Maier and J. K. Yang, *Nano Lett.*, 2011, **11**, 1323.
- ²⁸ S. F. Tan, L. Wu, J. K. Yang, P. Bai, M. Bosman and C. A. Nijhuis, *Science*, 2014, **343**, 1496; J. A. Scholl, A. García-Etxarri, A. L. Koh and J. A. Dionne, *Nano Lett.*, 2013, **13**, 564; J. A. Scholl, A. García-Etxarri, G. Aguirregabiria, R. Esteban, T. C. Narayan, A. L. Koh, J. Aizpurua and J. A. Dionne, *ACS Nano*, 2016, **10**, 1346.
- ²⁹ J. A. Scholl, A. L. Koh and J. A. Dionne, *Nature*, 2012, **483**, 421.
- ³⁰ G. C. Papavassiliou, *Prog. Solid State Chem.*, 1979, **12**, 185.
- ³¹ D. Rossouw and G. A. Botton, *Phys. Rev. Lett.*, 2013, **110**, 066801.
- ³² Ashley and L. Emerson, *Surf. Sci.*, 1974, **41**, 615.

-
- ³³ M. Bosman, E. Ye, S. F. Tan, C. A. Nijhuis, J. K. Yang, R. Marty, A. Mlayah, A. Arbouet, C. Girard and M.-Y. Han, *Sci. Rep.*, 2013, **3**, 1312.
- ³⁴ F. G. de Abajo and M. Kociak, *Phys. Rev. Lett.*, 2008, **100**, 106804; U. Hohenester, H. Ditlbacher and J. R. Krenn, *Phys. Rev. Lett.*, 2009, **103**, 106801.
- ³⁵ H. Cohen, P. Rez, T. Aoki, P. Crozier, N. Dellby, Z. Dellby, D. Gur, T. Lovejoy, K. March and M. Sarahan, *Microsc. Microanal.*, 2015, **21**, 661-662.
- ³⁶ J. Lecante, Y. Ballu and D. Newns, *Physical Review Letters*, 1977, **38**, 36.